Influenza A virus hemagglutinin remodels membranes into a vRNP clustering platform

Moritz Wachsmuth-melm
Heidelberg University Hospital
Sarah Peterl
Heidelberg University Hospital
Jana Makroczyová
Heidelberg University Hospital
Sílvia Vale-Costa
Universidade Católica Portuguesa
Maria-João Amorim
Instituto Gulbenkian de Ciência https://orcid.org/0000-0002-4129-6659
Petr Chlanda
petr.chlanda@bioquant.uni-heidelberg.de
University Hospital Heidelberg https://orcid.org/0000-0002-7782-2139

Biological Sciences - Article

Keywords:

Posted Date: April 10th, 2024

DOI: https://doi.org/10.21203/rs.3.rs-4008911/v1

Additional Declarations: There is **NO** Competing Interest.

Version of Record: A version of this preprint was published at Nature Communications on October 23rd, 2025. See the published version at https://doi.org/10.1038/s41467-025-65117-z.

Abstract

Pandemics caused by influenza A virus are associated with co-infections of zoonotic and human-adapted viruses. To form an infectious entity, the virus must incorporate eight different ribonucleoproteins (vRNPs) into virions budding at the plasma membrane. The process of vRNP clustering is poorly understood and has not been investigated at a molecular resolution. Here we employ *in situ* cryo-correlative light and electron microscopy at late stages of viral infection to identify hemagglutinin and neuraminidase as drivers of membrane remodelling. We show that hemagglutinin, but not neuraminidase-remodelled compartments serve as vRNP clustering platforms. Our nearest-neighbour analysis demonstrates that vRNPs cluster on hemagglutinin-remodelled membranes in a Rab11a-dependent manner. Additionally, we uncover that matrix protein 1 (M1) forms multi-layered cylindrical assemblies in the nucleus which restructure in the cytoplasm. Further, we show that M1 layer assembly precedes its attachment to the plasma membrane and M1 thereby coordinates the closure of the virion budding neck. In summary, we demonstrate that hemagglutinin is involved in intracellular vRNP clustering by inducing membrane remodelling to provide a large interaction surface. Thus hemagglutinin-membrane remodelling may play a role during vRNP sorting and reassortment that lead to the adaptation of zoonotic influenza A viruses.

Introduction

Viral genome segmentation is a strategy that allows for genome reassortment upon co-infection of two or more viruses. Genetic mixing via reassortment leads to antigenic shift — an increase in genetic diversity without the insertion of mutations into the genome, giving rise to novel, antigenically different viruses. An exemplary virus with a segmented genome is influenza A virus (IAV) which causes occasional pandemics that arise typically by zoonotic IAVs that cross the animal-human barrier and sustain a human-to-human transmission[1]. IAV is a membrane-enveloped pleomorphic virus that incorporates a negative-sense single-stranded RNA genome, divided into 8 segments. Each genome segment is encapsidated into a distinct viral ribonucleoprotein complex (vRNP) composed of nucleoprotein (NP) forming a helical rod-shaped complex with RNA[2–4]. To produce an infectious progeny, virions incorporate one copy of all 8 segments in a specific 7+1 configuration where one central vRNP is surrounded by 7 vRNPs[5,6]. Virus RNA replication takes place in the nucleus of an infected cell[7,8] where viral genome transcription utilises cap-snatched primers[9] and replication is driven by the tripartite polymerase complex composed of PA, PB1 and PB2 localised at the end of the vRNP. The polymerase forms a complex with complementary RNPs (cRNPs) encapsidating RNA of positive polarity serving as a template[10,11]. vRNP selective export depends on nuclear export protein (NEP) and chromosomal region maintenance 1 protein (CRM1)[12]. Upon export from the nucleus, vRNPs directly interact with Rab11a via the C-terminal domain of PB2[13]. This interaction was initially proposed as a mechanism for trafficking vRNPs to the plasma membrane, although it was immediately recognised that during infection Rab11a redistributed to form enlarged puncta that accumulated all vRNP types in the cytosol to be trafficked towards the plasma membrane[14–19]. Still, how and where during the trafficking vRNPs assemble into a

7+1-complex are among the longstanding questions in the influenza field. The answer to this question is pivotal to further understand molecular principles of IAV reassortment and zoonotic events. Multiple studies have used microscopy techniques to shed light on the mechanism underlying this process and several models have been proposed. Fluorescence In Situ Hybridization (FISH) and super-resolution microscopy studies have shown that vRNP clustering occurs en route to the budding site at the plasma membrane[20–22]. Recent studies revealed that vRNPs form liquid condensates that colocalize with Rab11a at endoplasmic reticulum (ER) exit sites[23] and influenza A virus infection remodelled ER which facilitate the transport of vRNPs[24]. However, due to the lack of context information during imaging in fluorescence microscopy and poor structural preservation of room temperature EM, single vRNPs have not yet been resolved and the site of vRNP 7+1 bundle formation and their association with membranous or membrane-less organelles remains elusive. IAV budding takes place at cholesterol-rich lipid raft domains formed at the plasma membrane[25,26]. This process is coordinated by matrix protein 1 (M1)[27] that forms a helical matrix layer underneath the viral envelope[28,29] and interacts with cytoplasmic tails of viral glycoproteins hemagglutinin (HA) and neuraminidase (NA)[30]. HA and NA undergo apical trafficking using Rab17 and Rab23 endosomal compartments[31,32]. Virus budding is concluded by membrane scission driven by the matrix protein 2 (M2) ion channel[33]. While it has been shown that the M1 layer interacts with vRNPs[33], this process is not fully understood and has not yet been studied at molecular resolution *in situ*.

Here we applied cellular cryo-ET to study cells infected with either H1N1 or H3N2 IAV and were able to visualize single vRNPs forming clusters in both the nucleus and cytosol. Intriguingly, we uncovered that HA and NA remodel host organelles by forming molecular zippers and discovered that vRNPs cluster on HA-remodelled organelles in a Rab11a-dependent manner. We show that vRNP density increases upon interaction with HA-remodelled membranes, thereby facilitating to probe for vRNP-vRNP interactions which may lead to sorting. Finally, our data uncover that M1 forms a multi-layered cylindrical structure and assembles the viral matrix layer that closes prior to budding neck formation and drives vRNP incorporation into budding virions.

Results and discussion

Hemagglutinin and neuraminidase induce membrane zippering in influenza A virus infected cells

To investigate the structural context of vRNP clustering sites, we performed *in situ* cryo-electron tomography (cryo-ET) of cryo-focused ion beam (cryo-FIB) milled A549 human lung epithelial cells infected with influenza A/Puerto Rico/8/1934 H1N1 virus (hereafter, PR8) or with a pandemic H3N2 strain A/Hong Kong/1/68 (hereafter, HK68). At 16 hours post-infection (hpi), we observed extensive membrane remodelling in all infected cells (fig. 1 a–d). Strikingly, we were able to detect two different types of membrane pairing, both resembling a zipper, forming membrane sheets and double membrane

vesicles of variable sizes. Since zippers could be distinguished by structurally distinct luminal protein arrays obvious in the tomograms, we classified them as zipper type I (fig. 1 a, b; supplementary video 1) and type II (fig. 1 c, d; supplementary video 2). While type I was formed by a single layer with C4 symmetry and membrane-to-membrane distance of 34 nm (fig. 1 e), type II consisted of two parallel arrays with membrane-to-membrane distance of 38 nm (fig. 1 h). Type I zippers were found only in HK68-infected cells, whereas type II zippers were found in all cells infected with PR8 and HK68.

Subtomogram averaging revealed that type I zippers were formed by neuraminidase (NA) forming a crystalline array with lateral spacing of 10 nm (fig. 1 e–g) and head-to-head angular displacement of 29° (fig. 1 k, l; supplementary video 3). Furthermore, we could demonstrate that type II zippers were formed by two opposing hemagglutinins (HA) in pre-fusion conformation (fig. 1 m, n). While the NA zipper was formed by NA-NA lateral interaction with alternating up and down NA headgroups, the HA zipper was formed by HA-HA ectodomain head-to-head interactions. Importantly, we could show that NA zippers can be connected to the plasma membrane (fig. 1 b), thus demonstrating that NA delivery to the plasma membrane in HK68 infected cells is driven by NA unzippering. Since NA zippers were not observed in PR8-infected cells, we sought to investigate possible structural differences between NA-PR8 (subtype 1) and NA-HK68 (subtype 2) in the NA-NA interacting regions. We used AlphaFold2[34] to predict HK68 and PR8 NA structures and fitted them into the subtomogram average (fig. 1 k, l). The prediction of the NA tetrameric headgroup corresponded well to experimentally determined NA but the stem region was predicted unstructured. The structure predictions revealed differences in surface charge distribution between PR8 and HK68 NA which could explain the lack of NA-NA zippering in PR8 infection (extended data fig. 1). Interestingly, a previous study showed that the expression of NA subtype 2 forms filamentous virus-like particles[27] indicating that NA subtype 2 can form organised arrays.

In contrast to the symmetric NA arrays, HA arrays showed HA-HA lateral spacing varying between 6 and 9 nm (fig. 1 i, j) which is consistent with HA-HA spacing on isolated virions[35,36]. HA-remodelled membranes were highly variable in size, with approximate diameters between 60 and 1220 nm (extended data fig. 3 a). Based on the extent of HA-zippering, we classified the HA-remodelled membranes into (i) single membranes coated with HA, (ii) double membranes with fully zippered HA and (iii) partial zippers displaying both phenotypes in the same membrane. 46% of observed HA-membranes were single membrane vesicles, whereas 28% were partially and 26% fully zippered double membranes that formed flat cisternae, autophagy-like compartments or double-membrane vesicles (extended data fig. 3 b). Since not all HA-containing organelles formed an HA-zipper (fig. 2 a, b; extended data fig. 2 a, b), we termed all HA-containing organelles HA-remodelled organelles and only those which show HA-HA zippering are termed as HA-zippers. Further, we also tested if HA-remodelling is dependent on other viral factors such as M2 which was shown to modulate autophagy in IAV-infected cells[37]. To this end, we performed *in situ* cryo-ET on HEK-293T cells transfected with HA, which showed that HA alone induces membrane remodelling indistinguishable from that observed in infected A549wt cells (extended data fig. 2 c). Overall, our data suggest that HA and NA form arrays inducing membrane remodelling. We propose

that the HA-induced membrane remodelling is a general hallmark of IAV infection and is solely induced by the HA glycoprotein.

vRNPs interact with HA-remodelled membranes

On the cytoplasmic sides of HA-remodelled membranes, we regularly observed cylindrical densities with helical striation reminiscent of vRNPs (fig. 1 h; supplementary video 2). Subtomogram averaging of the densities confirmed the double-helical structure with major and minor grooves of 85 Å and 65 Å (fig. 1 o) which is consistent with the previously published structure of vRNPs from isolated virions (fig. 1 p)[3]. vRNPs formed variably dense accumulations associated with 74% (n=109) of HA-remodelled membranes (extended data fig. 3 c) and only a single event was observed where vRNPs interacted with a vesicle not containing HA (extended data fig. 2 g). Interestingly, while vRNP accumulations were also observed at 8 hpi on 64% (n=36) of HA-remodelled membranes, we observed 8 events of vRNPs interacting with non-HA containing membranes showing budding of coated vesicles that likely represent ER exit-sites (extended data fig. 2 d). This indicates that vRNPs accumulate on HA-remodelled membranes during later stages of infection. In the case of HA-remodelled double membranes, vRNPs were found on both sides of the double membrane (fig. 1 c, h). A subset of vRNPs was directly in contact with HA-remodelled membranes, while vRNPs that were not directly interacting were found close to membrane-interacting vRNPs. Occasionally, vRNPs associated with HA-remodelled membranes formed a zone devoid of any cellular material such as ribosomes (extended data fig. 2 e, f), resembling a biomolecular condensate (supplementary videos 4, 5). Thus, our data agree with previously published studies[23,38–40] showing NP signal in the vicinity of ER-exit sites. NA-zippers found in HK68 infected cells (n=5) did not carry vRNPs besides one single example where vRNPs were found on a NA-zipper in a region devoid of NA (extended data fig. 2 h). Hence, our data demonstrate that HA-remodelled membranes play a major, yet unexplored role in cytoplasmic vRNP transport and clustering.

vRNP density is increased upon interaction with HA-remodelled membranes in a Rab11a-dependent manner

The small GTPase Rab11a has been extensively demonstrated to be essential for all stages of cytoplasmic vRNP transport[14,15,41]. This suggests that Rab11a may also be important for vRNP delivery to HA-remodelled membranes, or that HA-remodelled membranes themselves are the trafficking organelle delivering vRNPs to the plasma membrane. To test this hypothesis, we performed *in situ* cryo-ET on PR8-infected A549 cells constitutively overexpressing Rab11a wild-type (A549-Rab11wt) or Rab11a dominant-negative S25N mutant (hereafter, A549-Rab11dn) fused to green fluorescent protein (GFP)[42]. Both cell lines displayed the same HA-driven membrane remodelling as A549wt cells (fig. 2 a–c), with no significant differences in sizes of HA-remodelled membranes (extended data fig. 3 a). All aforementioned phenotypes of HA-zippering observed in A549wt cells were also found in A549-Rab11wt and A549-Rab11dn cells (extended data fig. 3 b). Notably, we observed a reduced association of vRNPs

with HA-remodelled membranes in A549-Rab11dn cells. In contrast to A549wt and A549-Rab11wt cells where 77% and 90% of analysed HA-remodelled membranes carried vRNPs, respectively, we observed only 40% of HA-remodelled membranes with vRNPs in A549-Rab11dn cells (extended data fig. 3 c). In addition, the number and density of vRNPs apparent in the tomograms were lower in A549-Rab11dn cells. Overall, our data show that vRNP accumulation on HA-remodelled membranes, but not the membrane remodelling itself, depends on the activity of Rab11a.

To gain insights into vRNP-vRNP interactions and their spatial distribution on HA-remodelled membranes, individual vRNPs were segmented and subjected to nearest-neighbour analysis (fig. 2 d–i). This allowed close inspection of vRNP-vRNP interactions in the context of membrane binding and quantitative assessment of the degree of clustering. The analysis confirms a significant increase in vRNP-vRNP distances in A549-Rab11dn cells compared to A549wt ($p = 4.9e-07$) and A549-Rab11wt ($p = 9.8e-08$) cells, even though the vRNP-membrane distances are only significantly different between A549-Rab11dn and -Rab11wt cells ($p = 1.7e-3$) (extended data fig. 3 d, e). These differences prompted us to investigate the clustering of vRNPs in more detail and validate clustering against a model with randomly distributed vRNPs. To this end, vRNP clusters were identified based on vicinity using a threshold of 4 nm. This revealed vRNP clusters of up to 15 vRNPs on HA-remodelled membranes in A549 and A549-Rab11wt cells (fig. 2 m, n) in contrast to only 4 vRNPs in A549-Rab11dn cells (fig. 2 o). Furthermore, increasing cluster size correlated with a shorter distance to HA-remodelled membranes (fig. 2 p). Clustering is reduced in a random vRNP model, independent of the vicinity threshold (extended data fig. 3 f, g). Overall, this data showed that HA-remodelled membranes serve as a platform that increases vRNP density at the HA-membrane surface.

We next aimed to substantiate our hypothesis that HA-remodelled membranes themselves are the Rab11a-positive trafficking organelle that delivers vRNPs to the plasma membrane. To this end, we tested the localization of Rab11a by immunofluorescence confocal microscopy on PR8 infected A549-Rab11wt cells immunostained against HA and NP, the latter as a proxy for vRNPs. In agreement with numerous previous studies[15,16,41], Rab11a and NP colocalized into large puncta distributed throughout the cytoplasm (extended data fig. 4 a–d). Surprisingly, we observed a low colocalization of HA with Rab11a (extended data fig. 4 e). Segmentation analysis revealed that 18.5% and 16.7% of HA puncta were interacting with Rab11a and NP puncta, respectively (extended data fig. 4 f). We therefore sought to validate the localization of Rab11a by performing cryo-correlative light and electron microscopy (CLEM) to localize GFP-Rab11a directly on cryo-FIB milled lamellae. This allowed us to direct cryo-ET data acquisition towards sites positive for GFP-Rab11a. Of 21 tomograms acquired at GFP-Rab11a positive areas, 86% contained HA-remodelled membranes (extended data fig. 4 g–j). Our data indicate that Rab11a binds to HA-remodelled membranes to deliver vRNPs.

M1 forms cylindrical assemblies in the nucleus which disassemble in the cytoplasm

In the current model of the IAV replication cycle, vRNPs are assembled in the nucleus of infected cells and exported to the cytoplasm in a complex with nuclear export protein (NEP) and M1[43]. In agreement with this model, we resolved a cluster of vRNPs in the nucleus of an A549 cell infected with PR8 at 8 hpi (fig. 3 a, b, g, h; supplementary video 6), confirming that vRNPs are fully assembled in the nucleus. In addition to vRNPs, our data on the nuclei of both PR8 and HK68 infected cells revealed hollow cylinders (fig. 3 c, d, i–l) with lengths between 65 and 285 nm (fig. 3 o) and inner diameters of 21 nm. Their outer diameter was highly variable, between 47 and 61 nm. Radial averaging of cylinder top views revealed 2 to 4 layers with a spacing of approx. 7 nm (fig. 3 p). These assemblies structurally correspond to previously reported M1 cylindrical structures assembled using a purified M1 protein at high salt concentration[28]. Similar cylindrical structures were also found inside virions upon acidification as an M1 layer disassembly product[44] and in H1N1 pdm2009 infected cells[45]. Collectively, this shows that M1 cylinders are present in cells infected by different IAV strains. Based on the measured nuclear pore complex (NPC) diameter in infected cells (110–155 nm), the M1 cylindrical assemblies can pass through the NPC. This is further supported by our data showing M1 cylindrical assemblies in the cytoplasm in the vicinity of HA-remodelled membranes (fig. 3 e, f, m, n; supplementary video 7) and close to viral budding sites (extended data fig. 5). Interestingly, cytoplasmic M1 assemblies were significantly shorter (fig. 3 o) and more often loosely coiled (nucleus: 8%; cytoplasm: 31%). This indicates that M1 forms cylindrical assemblies in the nucleus that upon export to the cytoplasm become unstable and disassemble. Multilayered M1 cylinders are stabilized by hydrophobic interactions between M1 N-terminal domains[28]. These are likely disrupted by M1 recruitment to the plasma membrane by M2[46], where interactions with the glycoproteins[47] and negatively charged phospholipids[48,49] stabilize a single-layer M1 matrix in the budding virions[29]. We propose that the transition from M1 cylinder to M1 layer is the inverse process to matrix layer disruption during virus entry at endosomal pH and delivers a large amount of building blocks to the plasma membrane to aid virus budding.

M1 layer formation drives the incorporation of vRNPs into the budding virions

To further shed light on the vRNP bundling process and the role of M1, we investigated IAV budding profiles by cryo-ET performed on cryo-FIB milled lamellae. Multiple stages of virion budding were observed (fig. 4 a, b): initial membrane bending induced by a small patch of a spherically curved M1 layer (4%, fig. 4 c, i); budding virions with incorporated vRNPs with open M1 layer (42%, fig. 4 d, e, j, k); closed or partially closed M1 layer (28%, fig. 4 f, l), fully assembled with budding neck (26%, fig. 4 g, m) and released viruses (not quantified, fig. 4 h, n). Importantly, cryo-ET allowed us to advance the mechanistic understanding of the budding process. In the virions with a partially closed M1 layer, the M1 layer was not fully attached to the membrane in the virions and had free curved ends interacting with vRNPs (fig. 4 e, k). This suggests that the M1 layer assembly precedes its attachment to the plasma membrane and M1 thereby drives the incorporation of vRNPs into the budding virions. This is in agreement with previous studies showing that budding of virus-like particles containing M1 layer is independent of vRNPs[27]. It is

noteworthy that vRNP bundles reminiscent of a 7+1 parallel configuration[5,6] were found neither on HA-remodelled membranes nor on the plasma membrane, but only in fully assembled virions. Hence, we propose that vRNPs only assemble in a parallel 7+1 bundle upon contact with a patch of M1 layer at the plasma membrane, presumably as a result of energetically most favourable packaging geometry within the M1 helically organized scaffold.

In summary, here presented data allowed us to uncover the interplay of several viral proteins during IAV late replication stages and propose a model (fig. 5). We identified HA as a mediator of membrane remodelling which provides a platform to probe vRNP-vRNP interactions in a Rab11a dependent manner. This provides a large membrane surface that could allow for vRNP sorting and clustering as previously determined by FISH and super-resolution microscopy[20,21]. This work reconciles previous contradicting models showing that vRNPs interact with membranes[24] but engage in vRNP-vRNP interactions to form membrane-associated biomolecular condensates[23]. Further studies will unravel the role of HA-induced membrane remodelling in co-infection and reassortment which is critical in leading to viral progeny with new antigenic footprint. In addition, pinpointing the HA-vRNP interaction and Rab11a recruitment to HA on the molecular level or abrogation of HA-induced membrane remodelling could lead to effective inhibition of vRNP clustering and virus replication. Interestingly, we show that HA compartments form closed double-membrane vesicles occasionally entrapping vRNPs (fig. 2; extended data fig. 2 a, b). This indicates that a fraction of vRNPs is released from the cell upon fusion of the double-membrane vesicle with the plasma membrane. We propose that this mechanism could lead to the formation of HA vesicles containing unspecifically incorporated vRNPs (fig. 5), which could serve as an immunological decoy and function similarly to defective interfering particles[50]. Finally, we report that M1 assembles into large cylindrical structures in the nucleus that disassemble in the cytoplasm, leading to the formation of the M1 layer, thus unravelling a potential pan-flu antiviral avenue by targeting M1 cylinder disassembly. Overall, this data highlights the multifunctional role of the M1 protein and uncovers the existence of the M1 cylindrical assemblies in infected cells, which has so far been identified only *in vitro* or inside virions at low pH.

Materials and methods

Cells

A549[51], obtained from American Type Culture Collection (ATCC), A549-Rab11KO[19] (kindly provided by Prof. Balaji Manicassami, University of Iowa, USA) A549-GFP-Rab11wt and A549-GFP-Rab11dn (kindly provided by Prof. João Amorim, Instituto Gulbenkian de Ciência, Portugal) cells were maintained in DMEM/F-12-GlutaMAX™, HEK-293T (ATCC) and MDCK (Prof. João Amorim) cells in DMEM-GlutaMAX™, both supplemented with 100 U/ml penicillin-streptomycin (P/S) and 10% (v/v) fetal bovine serum (FBS). Cells were subcultured twice per week. All incubation steps were performed at 37°C and 5% CO_2 unless otherwise noted.

Reverse genetics

Influenza A/Puerto Rico/8/1934 H1N1 and A/Hong Kong/1968 H3N2 were rescued using an 8-plasmid reverse genetics system. 2.7 × 10^6 HEK-293T cells were seeded in a 10 cm cell culture dish in 15 ml complete DMEM and incubated for 24 hours. Cells were then transfected with 8 plasmids, each corresponding to one genome segment. To this end, a transfection mix was prepared by mixing 1.5 ml OptiMEM with 1.875 µg of each plasmid (15 µg DNA in total) and adding 45 µl TransIT-LT1. The transfection mix was incubated for 20 minutes and carefully added on top of the cells. The cells were incubated for 24 hours. Next, the medium was exchanged 10 ml serum-free DMEM supplemented with 100 U/ml P/S, 1 µg/ml TPCK-trypsin and 0.3% BSA and 4 × 10^6 MDCK cells were seeded into the same cell culture dish. After 24 hours of incubation, the supernatant was harvested and centrifuged at 1000 rcf for 10 minutes to remove cell debris. The cleared supernatant was snap-frozen in liquid nitrogen and used as p0 virus stock for virus propagation.

Virus propagation

MDCK cells were grown in a T175 flask to confluency. P0 virus stock prepared above was thawed on ice and diluted in 10 ml DMEM supplemented with 100 U/ml P/S. MDCK cells were washed twice with PBS. The diluted virus was added to the cells and spread evenly by tilting the plate. Cells were incubated for 1 hour to allow virus uptake. Then, the cells were washed with infection medium (DMEM, 100 U/ml P/S, 1 µg/ml TPCK-trypsin and 0.3% BSA) and incubated in 40 ml infection medium. Cells were checked daily to watch for onset of cytopathic effect. Once most cells were detached, the supernatant was harvested, centrifuged at 1000 rcf for 10 minutes, aliquoted and snap-frozen in liquid nitrogen.

Virus titration by plaque assay

Into each well of two 6-well plates, 1 × 10^6 MDCK cells were seeded in 2 ml complete DMEM (100 U/ml P/S, 10% FBS) and incubated for 24 hours. The virus to be titrated was thawed on ice and serially diluted from 10^{-3} to 10^{-8} in 10-fold steps in serum-free DMEM. Cells were washed twice with PBS, then 900 µl virus dilution was added to each well such that each dilution was titrated in duplicates. After incubation for 1 hour, cells in each well were washed twice with PBS and overlaid with 3 ml DMEM supplemented with 1.2% Avicel-RC581, 0.14% BSA, 100 U/ml P/S and 1 µg/ml TPCK-trypsin. PR8 infected cells were incubated for two days, HK68 infected cells were incubated for four days to allow plaque formation.

To count plaques, the overlay medium was aspirated and cells were washed twice with PBS. Cells were chemically fixed for 30 minutes with 1 ml 1% glutaraldehyde in PBS per well. Each well was washed with PBS, then 200 µl Crystal Violet was added to each well. After 10 minutes, each well was washed twice with water to reveal the plaques. For each well, the titer was calculated using the formula . The final titer used in experiments was the mean of all titers from wells with a quantifiable number of plaques.

Immunofluorescence microscopy

5 × 10⁴ A549-Rab11wt or A549-Rab11dn cells were seeded onto 12 mm microscopy coverslips (NO. 1, Marienfeld) in a 24-well plate in 500 µl complete growth medium (DMEM/F-12, 10% FBS, 100 U/ml P/S) and incubated for 24 hours. For infection experiments, cells were washed twice with PBS and infected with PR8 or HK68 virus, respectively, diluted in FBS-free DMEM/F-12 with an MOI of 3 for 1 hour. Then, cells were washed twice with PBS and incubated in complete DMEM/F-12 for 16 hours. For transfection experiments, a transfection mix was prepared by mixing 50 µl OptiMEM with 0.5 µg plasmid and adding 1.5 µl Trans-IT LT1. The transfection mix was incubated for 20 minutes, then carefully added on top of the cells. The cells were then incubated for 24 hours. After incubation, cells were washed twice with PBS and fixed with 4% paraformaldehyde (PFA) in PBS for 15 minutes. Then, cells were washed twice with PBS and permeabilised with 0.2% Triton-X100 in PBS for 7 minutes. For blocking, cells were washed twice with PBS and incubated with blocking buffer (3% BSA, 0.1% Tween-20 in PBS) for 30 minutes. Then, the cells were washed twice with dilution buffer (1% BSA, 0.1% Tween-20 in PBS) and incubated with the primary antibodies (GeneTex GTX127357 rabbit anti-H1 and Sigma-Aldrich MAB8257 mouse anti-NP) in dilution buffer for 1 hour. The cells were washed twice with dilution buffer and incubated with the secondary antibodies (Invitrogen A11034 Alexa Fluor 488 goat anti-rabbit and Invitrogen A11030 Alexa Fluor 546 goat anti-mouse) and 300 nM 4’,6-diamidino-2-phenylindole (DAPI) in dilution buffer for 1 hour. Before mounting, cells were washed twice with PBS and once with water. The coverslips were then briefly blotted on the side and placed upside down on a 7 µl drop of Prolong Glass Antifade Mountant on a microscopy slide.

Confocal microscopy was performed on a Leica SP8 TCS laser scanning confocal microscope equipped with a 633/1.4 HC PL APO CS2 oil immersion objective. Lasers with wavelengths of 405 nm, 486 nm, 546 nm and 633 nm were used. Stacks were acquired with a pixel spacing of 180×180×300 nm. All data was deconvolved using AutoQuant X3 (Media Cybernetics) with number of iterations set to 100.

Colocalization analysis between was performed by calculating the Pearson’s and Manders’ colocalization coefficients were calculated using the JaCoP[52] ImageJ/FIJI plugin.

Confocal data were segmented in three dimensions using the surface segmentation tool in Imaris (Version 9.8.2, Oxford Instruments).

Plunge freezing of infected and transfected cells

22 × 10⁴ A549, A549-Rab11wt, A549-Rab11dn, A549-Rab11KO or HEK-293T cells were seeded onto Quantifoil R1.2/20 200 mesh grids in a 35 mm cell culture dish coated with SYLGARD™ 184 silicone elastomer. Both grids and dishes were glow-discharged and disinfected with 70% ethanol prior to cell seeding.

For infection, cells were washed twice with PBS and infected with PR8 or HK68 virus diluted in FBS-free DMEM/F-12 with an MOI of 3 for 1 hour. Then, cells were washed twice with PBS and incubated for 16 hours in complete DMEM/F-12. For transfection, a transfection mix was prepared by mixing 200 µl OptiMEM with 2 µg pCAGGS-HA(PR8) and adding 6 µl TransIT-LT1. The transfection mix was incubated for 20 minutes at room temperature and then carefully added on top of the cells. Transfected cells were incubated for 24 hours before plunge freezing.

Grids were removed from the medium and directly transferred to a Leica GP2 plunge freezer set to 80% chamber humidity and 37°C chamber temperature. A 3 µl drop of medium from the cell culture dish was added on the top side of the grid. Grids were blotted for 3 seconds and plunge frozen in liquid ethane at -185°C.

For CLEM experiments, cells were fixed by exchanging the medium with 4% PFA in PBS and incubating for 15 minutes at room temperature prior to blotting. Then, fixative was exchanged with PBS. Prior to blotting, a 3 µl drop of 10% glycerol in PBS was added onto the top side of the grid for 3 minutes to improve vitrification. Blotting and further steps were done as described above.

Cryo-FIB milling of infected and transfected cells

Grids were then clipped into ThermoFisher CryoFIB AutoGrids and loaded into an Aquilos 2 cryo-FIBSEM. Target cells were selected in Maps, lamellas were milled with autolamella[53].

Correlative light- and electron-microscopy

Cryo-FIB milled lamellae were imaged in a Zeiss LSM 900 Airyscan microscope equipped with a Linkam cryo-stage. First, an overview image was acquired using a 5× air objective in widefield mode. Of each lamella, a stack with 79.5×79.5×440 nm XYZ pixel spacing was acquired in super-resolution Airyscan mode with a Zeiss EC Epiplan-Neofluar 100×/0.75 DIC objective. Two channel images were acquired, GFP with a 488 nm laser set to 4% intensity and reflection mode using a 640 nm laser set to 0.02% intensity. Stacks were pre-processed using Zen blue (Zeiss) and motion-corrected using ImageJ/FIJI[54]. Then, maximum intensity projections were generated in ImageJ/FIJI.

Maximum intensity projections were aligned to maps of lamellae in SerialEM prior to tilt series acquisition[55]. For illustration purposes, maps were once more aligned to the same maps after tilt series acquisition using a custom napari[56] plugin.

Cryo-electron tomography

Data collection for cryo-ET was done using a Titan Krios Transmission Electron Microscope (TEM, ThermoFisher Scientific) operated at 300 keV and equipped with a BioQuantum® LS energy filter with a

slit width of 15 eV and K3 direct electron detector (Gatan) using SerialEM[55]. Montaged maps were acquired at 8700× magnification with pixel size 10.68 Å/px and approximate defocus of 80 µm. If applicable, light microscopy data was aligned to the maps in SerialEM using three registration points. Tilt series were acquired at 33,000× magnification with a pixel size of 2.671 Å/px at 2.5-4 µm defocus, with an electron dose of approximately 3.2 $e^{-}/Å^2$ per projection. A dose symmetric acquisition scheme was used with an effective tilt range of +68° to -52° in 3° increments[57] and tomograms were acquired in parallel with PACE-tomo[58].

Tomograms were reconstructed with a pixel size of 5.342 Å/px in Etomo. All tomograms were denoised with CryoCare[59] or IsoNet[60].

Subtomogram averaging

Tomograms reconstructed with a pixel size of 5.342 Å/px were imported into a Dynamo[61] catalogue. To generate an initial model, approx. 100 particles were manually picked using a dipole model. Then, coordinates were picked using either a surface model (HA and NA subtomogram average) or a filament model (vRNP subtomogram average). Particles were cropped using a box size of 128 pixels. Initial particle refinement was performed in Dynamo. For further refinement, tomograms and particle coordinates were imported into Relion 4.0.1.

Nearest-neighbour clustering analysis

Tomograms were scaled to a pixel-size of 10.684 Å/px and denoised using IsoNet[60]. Segmentations were done in IMOD: membranes were segmented as closed or open contours and meshed, vRNPs were segmented as open contours. Nearest-neighbour distances were calculated using MTK. The pairwise distances were then extracted from the resulting model file using a Python script. p-values were calculated with SciPy using a 2-sample Kolmogorov-Smirnov test.

To generate a random vRNP model, the segmentation models were shifted with MTK. All analyses were performed in the same way on the segmented and randomly shifted models.

For cluster identification, each vRNP and all neighbouring vRNPs closer than threshold t were defined as a cluster, which was iteratively expanded until no further vRNPs were closer than t. This was repeated for all vRNPs until every vRNP was assigned to a cluster.

All scripts were deposited on GitHub.

Declarations

Acknowledgements

We thank the Infectious Diseases Imaging Platform (IDIP) at the Center for Integrative Infectious Disease Research Heidelberg and the cryo-EM network at the Heidelberg University (HD-cryoNET) for support and assistance The authors gratefully acknowledge the data storage service SDS@hd supported by the Ministry of Science, Research, and the Arts Baden-Württemberg (MWK), the German Research Foundation (DFG) through grant INST 35/1314-1 FUGG and INST 35/1503-1 FUGG. We acknowledge the access and services provided by the Imaging Centre at the European Molecular Biology Laboratory (EMBL IC), generously supported by the Boehringer Ingelheim Foundation. We thank Prof. Balaji Manicassami for providing a A549-Rab11KO cell line.

Author contributions

Conceptualization: MWM and PC; Methodology: MWM, SP, JM, SVC, MJA; Investigation: MWM, SP, PC; Visualization: MWM, SP; Funding acquisition: PC, MJA; Project administration: PC; Supervision: MJA, PC; Writing - original draft: MWM, PC; Writing - review & editing: all

Funding

This work was supported by a research grant from the Chica and Heinz Schaller Foundation (Schaller Research Group Leader Programme) and by the Deutsche Forschungsgemeinschaft (DFG, German Research Foundation): P.C. project no. 240245660-SFB1129 and 437060729. Reagents for the project provided by MJA's laboratory were produced through funding by the European Research Council (ERC) under the European Union's Horizon 2020 research and innovation programme (grant agreement No 101001521). S.V.-C. salary supported by the portuguese Fundação para a Ciência e a Tecnologia (FCT): D.L.-57 and Auxiliary_Researcher/CEEC_INST2018/IBMC/2023/060.

Disclosure and competing interest statement

The authors declare that they have no conflict of interest.

Data availability

Electron tomography data will be deposited to EMDB and will be available upon publication. Additional data and material related to this publication may be obtained upon request.

References

1. Kumar, B. *et al.* The emerging influenza virus threat: Status and new prospects for its therapy and control. *Archives of Virology* **163**, 831–844 (2018).
2. Moeller, A., Kirchdoerfer, R. N., Potter, C. S., Carragher, B. & Wilson, I. A. Organization of the Influenza Virus Replication Machinery. *Science* **338**, 1631–1634 (2012).
3. Arranz, R. *et al.* The Structure of Native Influenza Virion Ribonucleoproteins. *Science* **338**, 1634–1637 (2012).

4. Coloma, R. *et al.* Structural insights into influenza A virus ribonucleoproteins reveal a processive helical track as transcription mechanism. *Nat Microbiol* **5**, 727–734 (2020).
5. Noda, T. *et al.* Architecture of ribonucleoprotein complexes in influenza A virus particles. *Nature* **439**, 490–492 (2006).
6. Noda, T. *et al.* Importance of the 1+7 configuration of ribonucleoprotein complexes for influenza A virus genome packaging. *Nat Commun* **9**, 54 (2018).
7. Krug, R. M. Influenza viral RNPs newly synthesized during the latent period of viral growth in MDCK cells. *Virology* **44**, 125–136 (1971).
8. Krug, R. M. Cytoplasmic and nucleoplasmic viral RNPs in influenza virus-infected MDCK cells. *Virology* **50**, 103–113 (1972).
9. Bouloy, M., Plotch, S. J. & Krug, R. M. Globin mRNAs are primers for the transcription of influenza viral RNA *in Vitro*. *Proc. Natl. Acad. Sci. U.S.A.* **75**, 4886–4890 (1978).
10. Fan, H. *et al.* Structures of influenza A virus RNA polymerase offer insight into viral genome replication. *Nature* **573**, 287–290 (2019).
11. Wandzik, J. M., Kouba, T. & Cusack, S. Structure and Function of Influenza Polymerase. *Cold Spring Harb Perspect Med* a038372 (2020) doi:10.1101/cshperspect.a038372.
12. Neumann, G. Influenza A virus NS2 protein mediates vRNP nuclear export through NES-independent interaction with hCRM1. *The EMBO Journal* **19**, 6751–6758 (2000).
13. Veler, H. *et al.* The C-Terminal Domains of the PB2 Subunit of the Influenza A Virus RNA Polymerase Directly Interact with Cellular GTPase Rab11a. *J Virol* **96**, e01979–21 (2022).
14. Eisfeld, A. J., Neumann, G. & Kawaoka, Y. Human Immunodeficiency Virus Rev-Binding Protein Is Essential for Influenza A Virus Replication and Promotes Genome Trafficking in Late-Stage Infection. *Journal of Virology* **85**, 9588–9598 (2011).
15. Amorim, M. J. *et al.* A Rab11- and Microtubule-Dependent Mechanism for Cytoplasmic Transport of Influenza A Virus Viral RNA. *Journal of Virology* **85**, 4143–4156 (2011).
16. Bruce, E. A., Digard, P. & Stuart, A. D. The Rab11 Pathway Is Required for Influenza A Virus Budding and Filament Formation. *Journal of Virology* **84**, 5848–5859 (2010).
17. Amorim, M. J. A comprehensive review on the interaction between the host GTPase Rab11 and influenza A virus. *Frontiers in Cell and Developmental Biology* **6**, 1–14 (2019).
18. Bhagwat, A. R. *et al.* Quantitative live cell imaging reveals influenza virus manipulation of Rab11A transport through reduced dynein association. *Nat Commun* **11**, 23 (2020).
19. Han, J. *et al.* Host factor Rab11a is critical for efficient assembly of influenza A virus genomic segments. *PLoS Pathog* **17**, e1009517 (2021).
20. Lakdawala, S. S. *et al.* Influenza a virus assembly intermediates fuse in the cytoplasm. *PLoS Pathog.* **10**, e1003971 (2014).
21. Haralampiev, I. *et al.* Selective flexible packaging pathways of the segmented genome of influenza A virus. *Nat Commun* **11**, 4355 (2020).

22. Touizer, E., Sieben, C., Henriques, R., Marsh, M. & Laine, R. F. Application of Super-Resolution and Advanced Quantitative Microscopy to the Spatio-Temporal Analysis of Influenza Virus Replication. *Viruses* **13**, 233 (2021).
23. Alenquer, M. *et al.* Influenza A virus ribonucleoproteins form liquid organelles at endoplasmic reticulum exit sites. *Nature Communications* **10**, 1629–1629 (2019).
24. De Castro Martin, I. F. *et al.* Influenza virus genome reaches the plasma membrane via a modified endoplasmic reticulum and Rab11-dependent vesicles. *Nature Communications* **8**, 1396–1396 (2017).
25. Zhang, J., Pekosz, A. & Lamb, R. A. Influenza Virus Assembly and Lipid Raft Microdomains: A Role for the Cytoplasmic Tails of the Spike Glycoproteins. *J Virol* **74**, 4634–4644 (2000).
26. Takeda, M., Leser, G. P., Russell, C. J. & Lamb, R. A. Influenza virus hemagglutinin concentrates in lipid raft microdomains for efficient viral fusion. *Proceedings of the National Academy of Sciences of the United States of America* **100**, 14610–14617 (2003).
27. Chlanda, P. *et al.* Structural Analysis of the Roles of Influenza A Virus Membrane-Associated Proteins in Assembly and Morphology. *J. Virol.* **89**, 8957–8966 (2015).
28. Selzer, L., Su, Z., Pintilie, G. D., Chiu, W. & Kirkegaard, K. Full-length three-dimensional structure of the influenza A virus M1 protein and its organization into a matrix layer. *PLoS Biol* **18**, e3000827 (2020).
29. Peukes, J. *et al.* The native structure of the assembled matrix protein 1 of influenza A virus. *Nature* **587**, 495–498 (2020).
30. Chlanda, P. & Zimmerberg, J. Protein-lipid interactions critical to replication of the influenza A virus. *FEBS Lett* **590**, 1940–1954 (2016).
31. Barman, S. & Nayak, D. P. Analysis of the Transmembrane Domain of Influenza Virus Neuraminidase, a Type II Transmembrane Glycoprotein, for Apical Sorting and Raft Association. *J Virol* **74**, 6538–6545 (2000).
32. Sato, R. *et al.* Apical Trafficking Pathways of Influenza A Virus HA and NA via Rab17- and Rab23-Positive Compartments. *Front. Microbiol.* **10**, 1857 (2019).
33. Rossman, J. S. & Lamb, R. A. Influenza virus assembly and budding. *Virology* **411**, 229–236 (2011).
34. Mirdita, M. *et al.* ColabFold: Making protein folding accessible to all. *Nat Methods* **19**, 679–682 (2022).
35. Chlanda, P. *et al.* The hemifusion structure induced by influenza virus haemagglutinin is determined by physical properties of the target membranes. *Nat Microbiol* **1**, 16050 (2016).
36. Huang, Q. J. *et al.* Quantitative structural analysis of influenza virus by cryo-electron tomography and convolutional neural networks. *Structure* **30**, 777–786.e3 (2022).
37. Beale, R. *et al.* A LC3-Interacting Motif in the Influenza A Virus M2 Protein Is Required to Subvert Autophagy and Maintain Virion Stability. *Cell Host & Microbe* **15**, 239–247 (2014).
38. Vale-Costa, S. *et al.* Influenza A virus ribonucleoproteins modulate host recycling by competing with Rab11 effectors. *Journal of Cell Science* jcs.188409 (2016) doi:10.1242/jcs.188409.

39. Vale-Costa, S. *et al.* ATG9A regulates the dissociation of recycling endosomes from microtubules to form liquid influenza A virus inclusions. *PLoS Biol* **21**, e3002290 (2023).
40. Etibor, T. A. *et al.* Defining basic rules for hardening influenza A virus liquid condensates. *eLife* **12**, e85182 (2023).
41. Momose, F. *et al.* Apical transport of influenza A virus ribonucleoprotein requires Rab11-positive recycling endosome. *PLoS ONE* **6**, 1–15 (2011).
42. Dale, L. B., Seachrist, J. L., Babwah, A. V. & Ferguson, S. S. G. Regulation of Angiotensin II Type 1A Receptor Intracellular Retention, Degradation, and Recycling by Rab5, Rab7, and Rab11 GTPases. *Journal of Biological Chemistry* **279**, 13110–13118 (2004).
43. Noton, S. L. *et al.* Identification of the domains of the influenza A virus M1 matrix protein required for NP binding, oligomerization and incorporation into virions. *Journal of General Virology* **88**, 2280–2290 (2007).
44. Calder, L. J., Wasilewski, S., Berriman, J. A. & Rosenthal, P. B. Structural organization of a filamentous influenza A virus. *Proceedings of the National Academy of Sciences of the United States of America* **107**, 10685–10690 (2010).
45. Terrier, O. *et al.* The influenza fingerprints: NS1 and M1 proteins contribute to specific host cell ultrastructure signatures upon infection by different influenza A viruses. *Virology* **432**, 204–218 (2012).
46. Petrich, A., Dunsing, V., Bobone, S. & Chiantia, S. Influenza A M2 recruits M1 to the plasma membrane: A fluorescence fluctuation microscopy study. *Biophysical Journal* **120**, 5478–5490 (2021).
47. Barman, S., Ali, A., Hui, E. K.-W., Adhikary, L. & Nayak, D. P. Transport of viral proteins to the apical membranes and interaction of matrix protein with glycoproteins in the assembly of influenza viruses. *Virus Research* **77**, 61–69 (2001).
48. Bobone, S. *et al.* Phosphatidylserine Lateral Organization Influences the Interaction of Influenza Virus Matrix Protein 1 with Lipid Membranes. *J Virol* **91**, e00267–17 (2017).
49. Raut, P. *et al.* Phosphatidylinositol 4,5-Bisphosphate Mediates the Co-Distribution of Influenza A Hemagglutinin and Matrix Protein M1 at the Plasma Membrane. *Viruses* **14**, 2509 (2022).
50. Alnaji, F. G. & Brooke, C. B. Influenza virus DI particles: Defective interfering or delightfully interesting? *PLoS Pathog* **16**, e1008436 (2020).
51. Giard, D. J. *et al.* In Vitro Cultivation of Human Tumors: Establishment of Cell Lines Derived From a Series of Solid Tumors2. *JNCI: Journal of the National Cancer Institute* **51**, 1417–1423 (1973).
52. Bolte, S. & Cordelières, F. P. A guided tour into subcellular colocalization analysis in light microscopy. *Journal of Microscopy* **224**, 213–232 (2006).
53. Buckley, G. *et al.* Automated cryo-lamella preparation for high-throughput in-situ structural biology. *Journal of Structural Biology* **210**, (2020).

54. Schneider, C. A., Rasband, W. S. & Eliceiri, K. W. NIH Image to ImageJ: 25 years of image analysis. *Nat Methods* **9**, 671–675 (2012).
55. Mastronarde, D. N. Automated electron microscope tomography using robust prediction of specimen movements. *Journal of Structural Biology* **152**, 36–51 (2005).
56. Ahlers, J. *et al.* Napari: A multi-dimensional image viewer for Python. Zenodo https://doi.org/10.5281/ZENODO.8115575 (2023).
57. Hagen, W. J. H., Wan, W. & Briggs, J. A. G. Implementation of a cryo-electron tomography tilt-scheme optimized for high resolution subtomogram averaging. *Journal of Structural Biology* **197**, 191–198 (2017).
58. Eisenstein, F. *et al.* Parallel cryo electron tomography on in situ lamellae. *Nat Methods* (2022) doi:10.1038/s41592-022-01690-1.
59. Buchholz, T.-O. *et al.* Content-aware image restoration for electron microscopy. *Methods in Cell Biology* **152**, 277–289 (2019).
60. Liu, Y.-T. *et al. Isotropic Reconstruction of Electron Tomograms with Deep Learning*. http://biorxiv.org/lookup/doi/10.1101/2021.07.17.452128 (2021) doi:10.1101/2021.07.17.452128.
61. Castaño-Díez, D., Kudryashev, M., Arheit, M. & Stahlberg, H. Dynamo: A flexible, user-friendly development tool for subtomogram averaging of cryo-EM data in high-performance computing environments. *Journal of Structural Biology* **178**, 139–151 (2012).

Figures

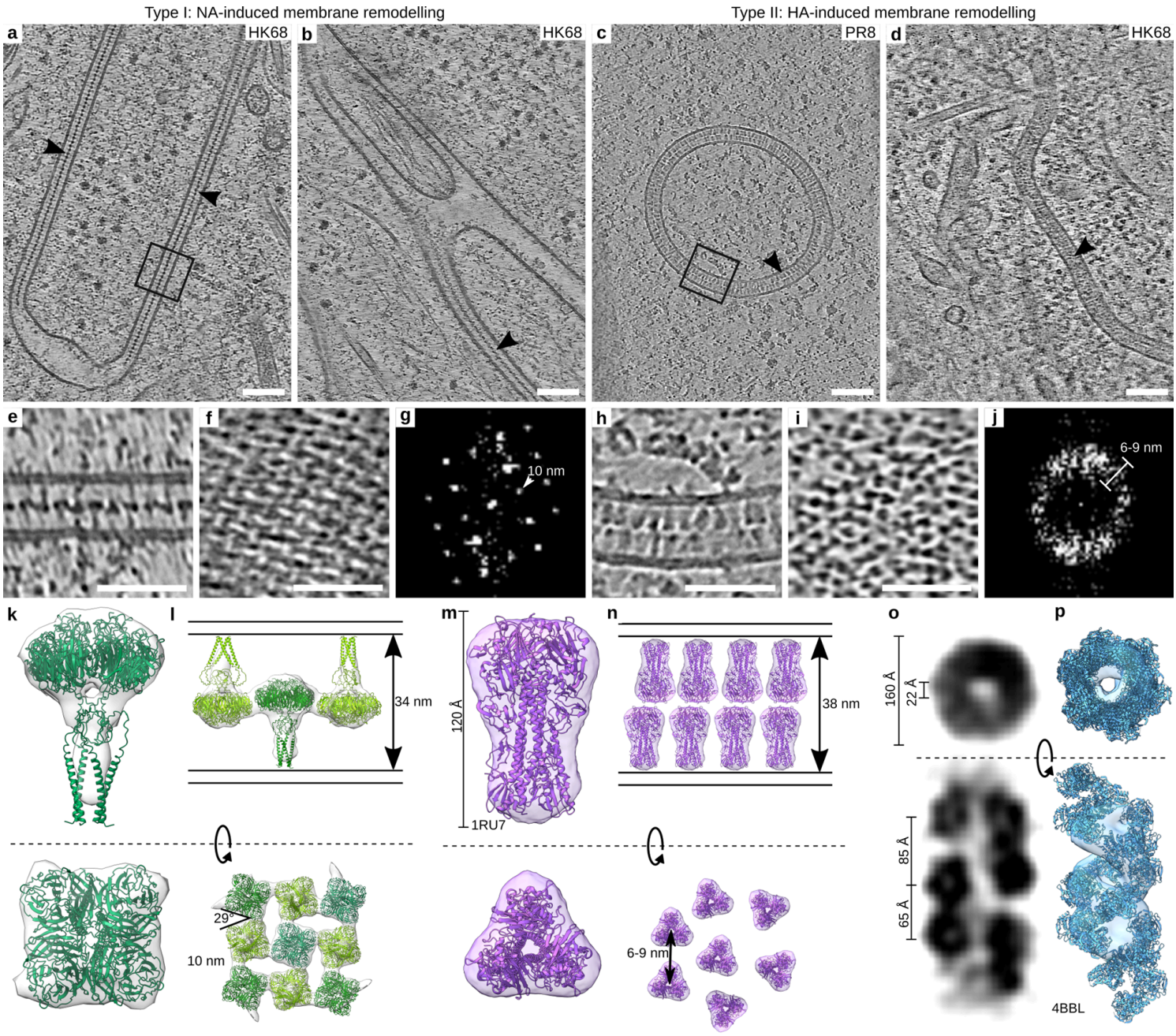

Figure 1

Influenza A virus glycoproteins form molecular zippers to remodel host membranes. A – D Representative slices through cryo-electron tomograms of A549 cells infected with PR8 or HK68 at 16 hours post-infection. HA and NA-remodelled membranes are indicated by arrowheads. **E**Magnified slice through the tomogram of the NA-zipper shown in A. **F**Representative slice of a tomogram showing the cross-section of the NA array. **G**Fast Fourier Transformation (FFT) of F indicating the NA-NA spacing of 10 nm. **H**Magnified slice through the tomogram of the HA-zipper shown in C. **I**Representative slice of a tomogram showing the cross-section of the HA array. **J**Fast Fourier Transformation (FFT) of F indicating the HA-HA spacing of 6 to 9 nm. **K, L** Subtomogram average of individual NA and a subtomogram average of NA array fitted with predicted NA structure delivered from AlphaFold2 with black lines indicating membrane bilayers. **M, N** Subtomogram average of HA with the fitted structure determined

experimentally (PDB: 1RU7) and a model of the HA zipper with black lines indicating membrane bilayers. **O** Slice through the subtomogram average of vRNPs showing the major and minor groove. **P**Subtomogram average shown in O with the fitted experimentally determined vRNP structure (PDB: 4BBL). Scale bars: A–D 100 nm; E, F, H, I 50 nm.

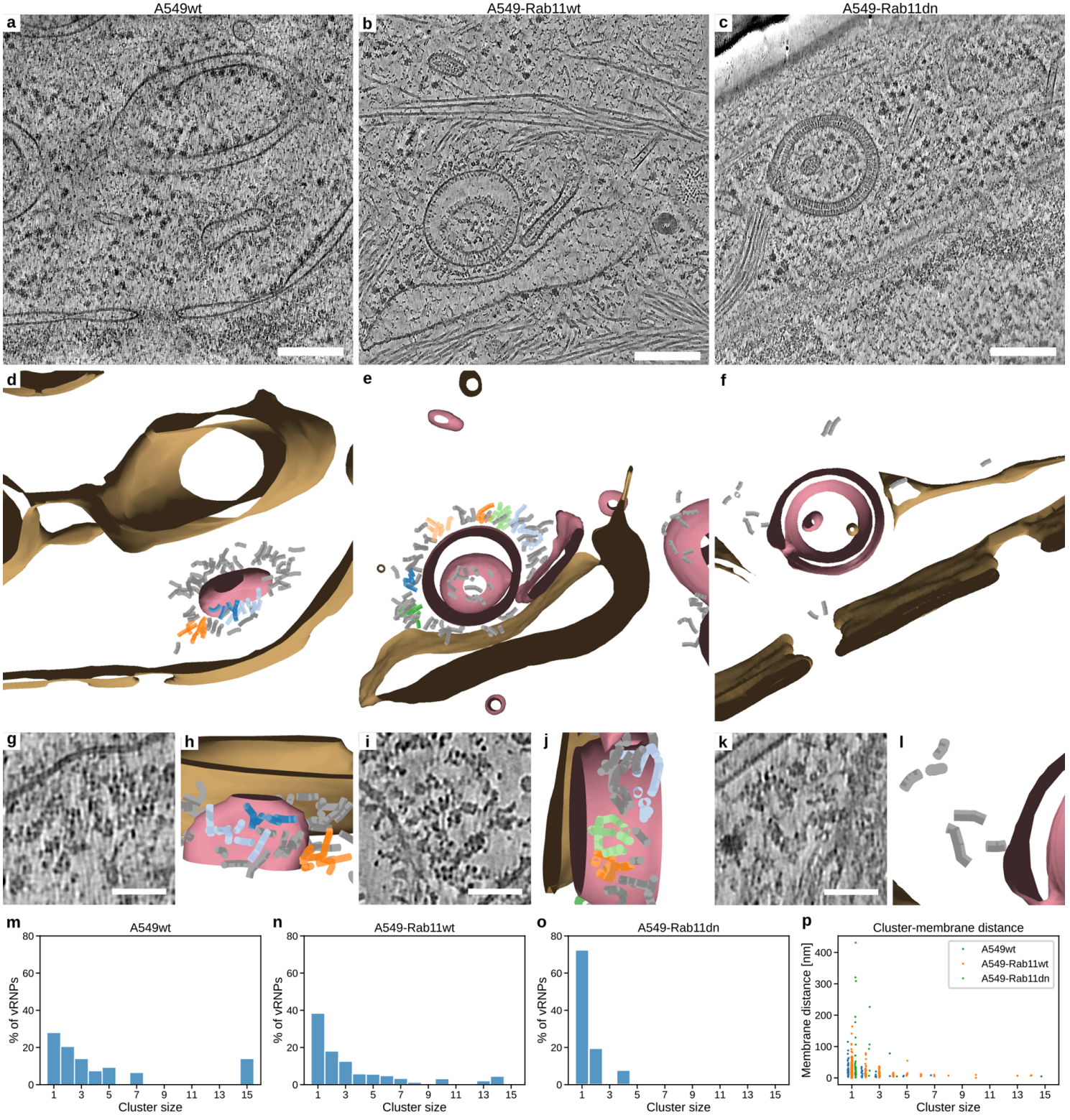

Figure 2

vRNPs cluster in the vicinity of HA-remodelled membranes in a Rab11a dependent manner. A–C Representative slices through cryo-electron tomograms of an A549wt (A), A549-Rab11wt (B) and A549-Rab11dn (C) cell each showing an HA-remodelled membrane and vRNPs. **D–F**Segmentations of the tomograms shown in A–C depicting HA-remodelled membranes (pink), other membranes (brown) and vRNPs (various colours). vRNPs part of a cluster of one or two vRNPs are coloured gray, while larger vRNP clusters are each assigned a different colour. **G–L** Magnified views of the tomograms and segmentations shown in A–F displaying vRNP clusters on HA-remodelled membranes. Segmentations are rotated to better highlight vRNP clustering. **M–O**Distribution of vRNP cluster sizes in A549wt (N), A549-Rab11wt (O) and A549-Rab11dn (P) cells. **P** Shortest distance to HA-remodelled membranes for each vRNP cluster. Scale bars: A–C 200 nm; G, I, K 50 nm.

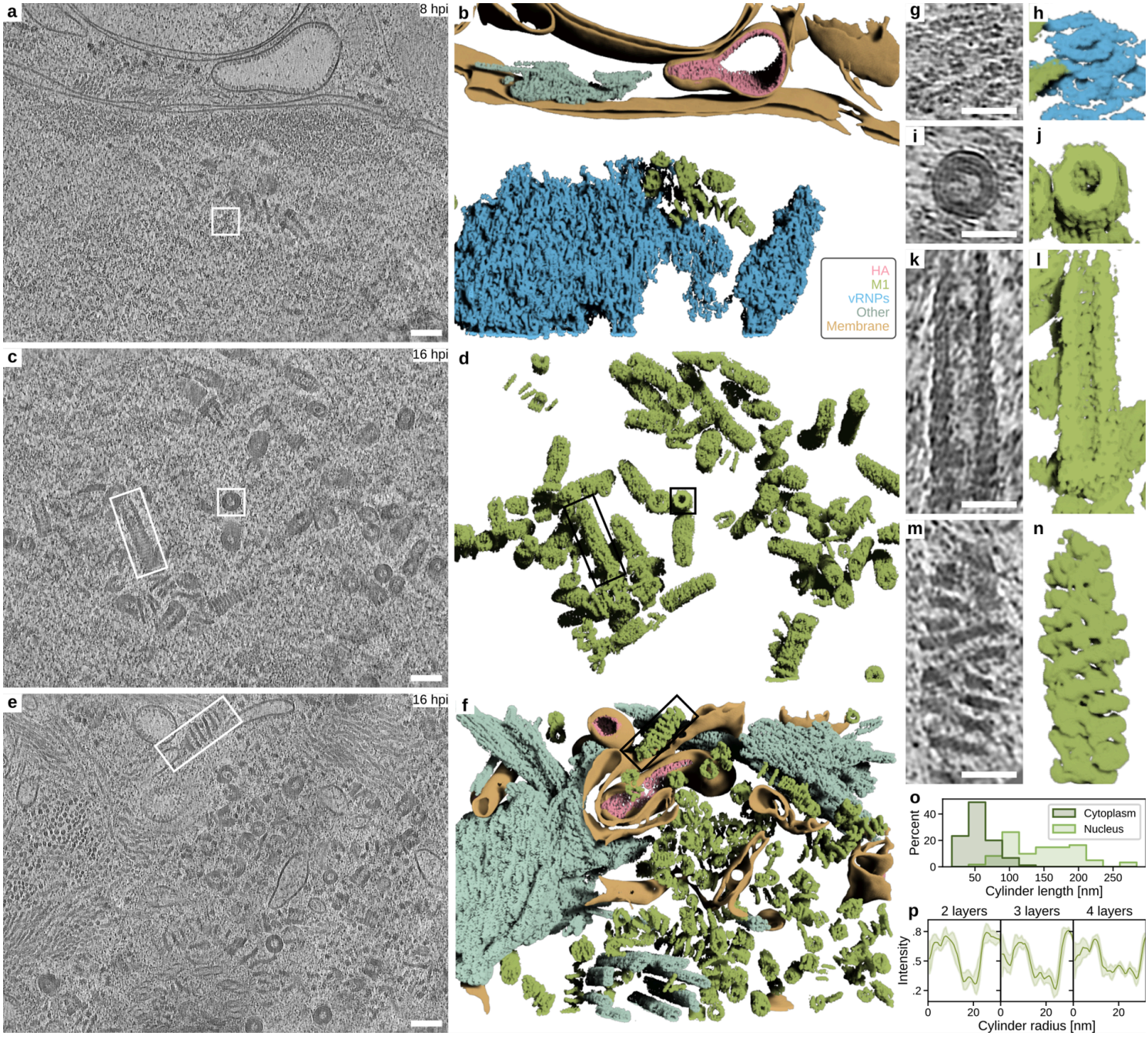

Figure 3

M1 forms cylindrical assemblies in the nucleus that disassemble in the cytoplasm. A, C, E Representative slices through cryo-electron tomograms of A549wt cells infected with PR8 at 8 (A) and 16 (B, C) hours post-infection showing a cluster of compact M1 cylindrical assemblies in the nucleus (A, B) and loosely coiled assemblies inside the cytoplasm (C). **B, D, F** Segmentations of the tomograms shown in A, C, E. Legend is shown in B. **G–N** Magnified areas of tomograms and segmentations indicated by white rectangles in A, C, E showing vRNPs interacting with M1 (G, H), top and side views of condensed M1 cylinders (I–L) and a side view of a loosely coiled M1 cylinder (M, N). **O** Lengths of condensed M1 cylinders in nucleoplasm (light green) and cytoplasm (dark green). **P** Radial profiles of condensed M1 cylinders of different diameters revealing different numbers of layers. M1 cylinders with 4 layers are more heterogeneous, hence the fourth layer is not visible in the radial average from multiple slices, yet each individual slice has 4 layers. Scale bars: A, C, E 100 nm; G, I, K, M 50 nm.

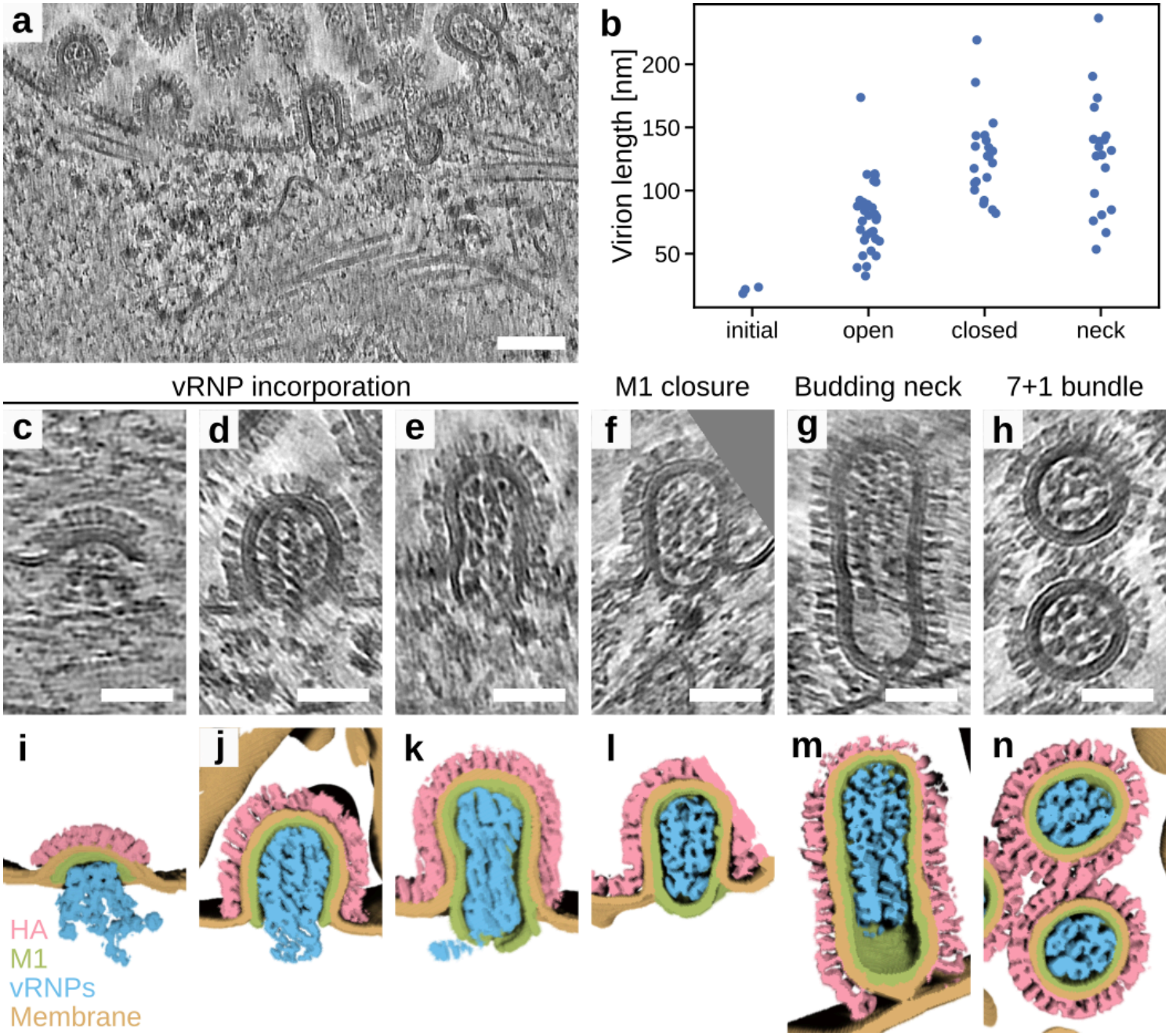

Figure 4

M1 layer formation drives incorporation of vRNPs into the budding virions A Slice through a tomogram of an A549wt cell infected with PR8 at 16 hpi. Numerous viruses are budding or have already successfully budded. **B** Quantification of protruding PR8 virion lengths during budding per stage of budding. **C–H** Representative slices through tomograms of budding viruses at different stages of budding, from initial (C) over open M1 layer (D, E), closed M1 layer (F), budding neck (G) and finished budding (H). **I–N** Segmentations of the areas shown in C–H. Scale bars: A 100 nm; C–H 50 nm.

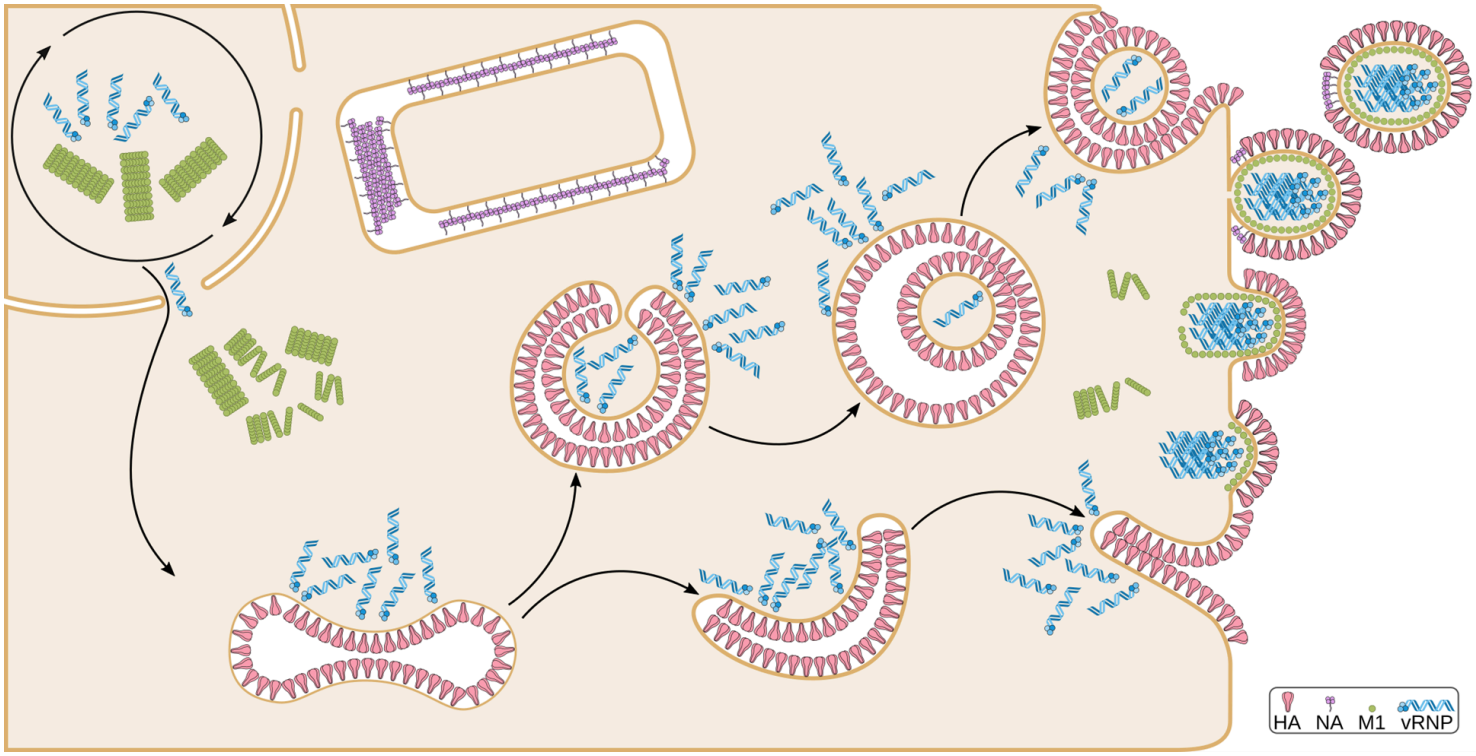

Figure 5

Model of IAV vRNP trafficking. vRNPs are assembled in the nucleus and exported to the cytoplasm where they accumulate on HA-remodelled membranes which serve as clustering platforms in a Rab11 dependent manner. HA-remodelled membranes are trafficked to the plasma membrane where they fuse, delivering vRNPs and HA to the sites of budding. M1 cylinders disassemble in the cytoplasm delivering the building blocks for the formation of the M1 layer, which drives the incorporation of vRNPs into budding virions. The M1 layer closes, driving the formation of a budding neck. Fully closed HA-zippers that fuse with the plasma membrane release HA-coated vesicles that could serve a similar purpose as defective interfering particles. NA-remodelled membranes fuse with plasma membrane to deliver NA.

Supplementary Files

This is a list of supplementary files associated with this preprint. Click to download.

- suppmovie1.mp4
- suppmovie2.mp4

- suppmovie3.mp4
- suppmovie4.mp4
- suppmovie5.mp4
- suppmovie6.mp4
- suppmovie7.mp4
- Extendeddata.docx